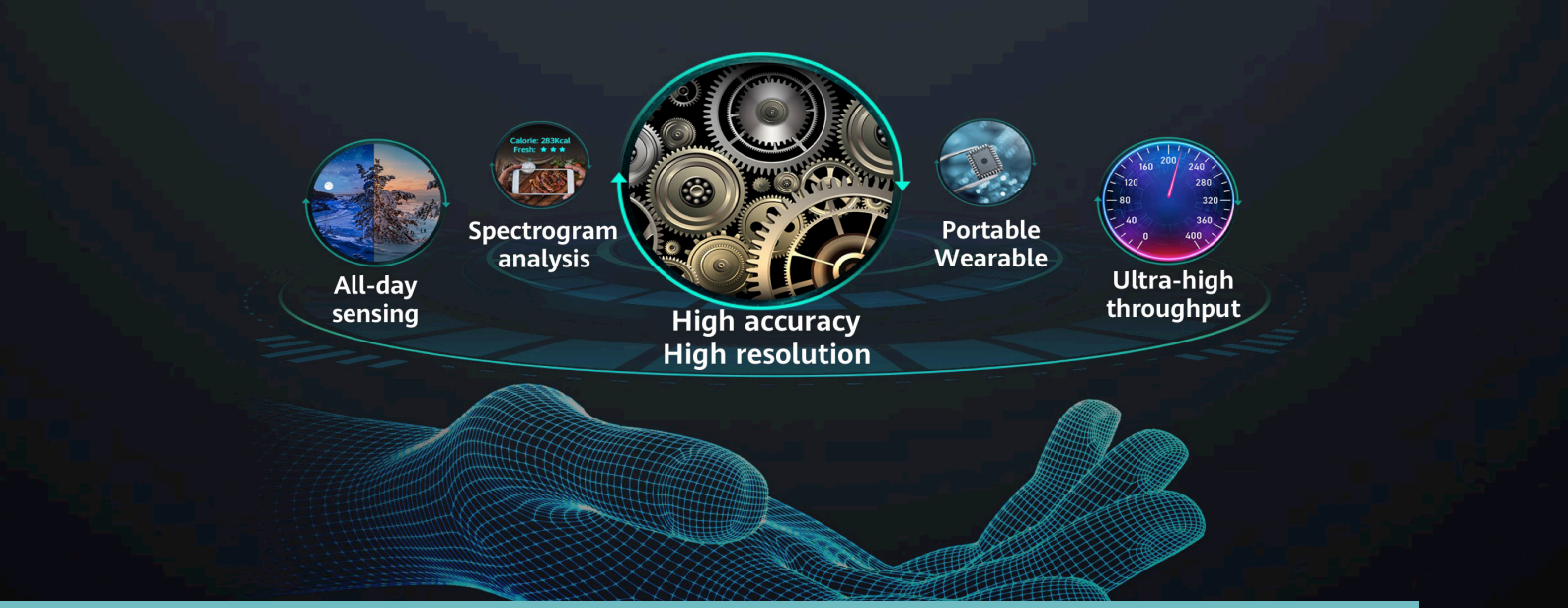

Terahertz Sensing and Communication Towards Future Intelligence Connected Networks

Guangjian Wang [1], Huanhuan Gu [2], Xianjin Li [1], Ziming Yu [1], Oupeng Li [1], Qiao Liu [1], Kun Zeng [1], Jia He [1], Yan Chen [2], Jianmin Lu [1], Wen Tong [2], David Wessel [2]

[1] Wireless Technology Lab

[2] Ottawa Wireless Advanced System Competency Centre

Abstract

The terahertz (THz) technologies are extremely promising for future 6G wireless communication and sensing systems because of the advantages of ultra-wide available bandwidth. However, the increased operating frequency and bandwidth pose higher requirements in terms of propagation channel modeling, new transmission technologies, high performance components, and signal processing complexity. Therefore, the challenge lies in how to achieve system demands as well as improve the system data rate and sensing resolution with limited hardware complexity and power consumption.

In this paper, the latest progress on spectrum and potential application scenarios for the THz band are examined. A hybrid channel modeling framework for the THz band is proposed to improve the accuracy and efficiency of the modeling. The potential intermediate radio frequency (IRF) architecture, key components, and antenna and integration technologies have also been investigated. In particular, the THz subsystem with silicon and III-V compound semiconductor material heterogeneous integration is proposed to promote the performance by utilizing the advantages of different processes and materials. Finally, the prototype and measurement campaign are conducted, which illustrate the advantages of the THz band for high throughput communication and high resolution sensing scenarios. A variety of measurement campaign examples show 210 Gbit/s data transmission rate at 330 m distance, and up to 3 mm invisible imaging, which is the highest performance in this field.

Keywords

channel model, phased array, reconfigurable intelligent surface, THz, THz antenna, THz integration technologies, integrated sensing and communication, wireless communication

1 Introduction

With the rapid development of wireless cellular communication from 1G to 5G, it is not just humans that are being better connected, but also an increasing number of intelligent things such as industrial equipment, cars, sensors, and home devices. This trend will continue beyond 2030, leading to intelligent connection of everything, anywhere, all-time [1]. If these intelligent things also have the capability of sensing their surroundings and sharing this information with other intelligent things, this will make connections even more intelligent. Joint radar and communication technology have been considered in this regard. Co-located radar and communication systems have been emphasized for the goal of minimizing interference to each other in previous research [2–3]. However, it has stringent requirements on the information exchange between these two systems, hence leading to limitations in practice. Effective integrated sensing and communication (ISAC) systems, including those that are loosely coupled to those fully integrated, are expected to reduce the system size and information exchange latency between the co-located radar and communication systems. With each new generation, higher spectrum with larger bandwidth is utilized. This is also beneficial for sensing. If we can make THz work for 6G, many new opportunities will be within our grasp. For the reasons previously stated, we believe the sensing will be one of key new services for 6G in addition to the continued expansion of 5G services.

To this end, the terahertz (THz) band (0.1–10 THz) is one of many promising pillar technologies that meets the requirements of 6G for 2030 and beyond, accommodating a massive number of connected devices and featuring ultra-high user data rates in the order of terabit per second (Tbit/s) [1]. This is because the THz band has ultra-large available bandwidth resources and ultra-high communication rates. Therefore, THz communication is considered as an important alternative air interface technology for achieving Tbit/s communication rate. It is also expected to be applied to scenarios such as holographic communication, small-scale communication, ultra-large-capacity data backhaul, and short-distance ultra-high-speed transmission. In addition, high-precision positioning and high-resolution sensing imaging of a network and/or a terminal device are performed by using a feature of an extremely large bandwidth, which is also an expansion direction of a THz communication application [4].

As mentioned previously, THz can provide high-quality imaging resolution equivalent to optics (about 100 microns). THz waves can penetrate many infrared opaque materials such as paper, plastics, ceramics and semiconductors. They can interact with molecular hydrogen bonds or van der Waals forces without any ionizing radiation and can be used for spectroscopic identification of organic materials. Terahertz photons have low energy (1 THz is equivalent to 4 meV) and are not harmful to human beings, unlike high energy X-rays. The vibrational and rotational energy levels of molecules, as well as the phonon vibrational energy levels of semiconductors and superconducting materials are all within the THz band, so THz waves have great advantages in spectral analysis and material identification. Because THz can be used for both communication and sensing, it is a strong candidate for ISAC [5].

Compared with millimeter waves and microwaves in low frequency bands and visible light in high frequency bands, the THz channel characteristics are quite different. Compared with millimeter waves, THz waves have stronger frequency selectivity, more obvious scattering effect, and larger transmission loss. Compared with a light wave, a THz wave has less path loss, stronger volatility, stronger reflected energy, and is less likely to be blocked. Therefore, the existing channel models and measurement methods of millimeter waves, microwaves, and visible light systems cannot be directly applied to the THz band, which highlights the necessity of developing THz channel measurement instruments. In the field of wireless channel modeling, there are two modeling methods. One is statistical channel modeling methodology based on measured data, and the other is deterministic channel modeling methodology based on ray tracing or electromagnetic (EM) field boundary solving theory [6]. Statistical channel modeling theory is widely used in mobile communication standard channel modeling scenarios [7], such as the 3GPP standard channel model. However, with the continuous enrichment of next-generation mobile communication scenarios, the demand for a new spectrum increases, and a statistical channel modeling method cannot completely meet the new channel requirements. Therefore, deterministic channel modeling methods are gradually being studied, and high-precision channel modeling in specific scenarios is carried out by

using computational electromagnetics (CEM) methods [8].

The device based on the THz semiconductor technology mainly refers to a transistor in the THz frequency band. The solid-state circuit based on the solid-state device can implement the THz source and perform frequency mixing, frequency multiplication, and amplification on the THz signal to generate and detect the THz wave at a specific frequency [9].

The Schottky barrier diode (SBD) can work at normal temperature, and has a low turn-on voltage and a very short reverse recovery time. At present, the SBD in the THz band is mainly based on GaAs material because of its high saturation electron rate and electron mobility. GaAs-based SBD is used in THz solid-state active circuit and represented by American VDI Company since 1960s, which has been very mature and industrialized. Currently, the cutoff frequency of the component is higher than 30 THz, and the frequency mixer and frequency multiplier basically cover the THz band.

Chip integration has become the most important research direction of THz semiconductor technology. Based on semiconductor materials, semiconductor devices used in THz band amplifiers can be divided into two types: Si-based devices and III-V compound-based devices [10–11]. Si-based devices are mainly complementary metal–oxide–semiconductor (CMOS) devices and SiGe bipolar complementary metal-oxide-semiconductor (BiCMOS) devices. Group III-V compound devices include GaAs pseudomorphic high-electron-mobility transistor (PHEMT), GaAs metamorphic high-electron-mobility transistor (MHEMT), InP high-electron-mobility transistor (HEMT), InP heterojunction bipolar transistor (HBT), and GaN HEMT.

The selection of the various process and material properties for THz devices is primarily based on the characteristic frequency and cutoff frequency. To select the right technology for THz applications, many parameters must be considered, such as cost, output power, efficiency, maturity of interconnection and packaging technologies, and integration capabilities. In the THz band, a large-scale antenna array is usually required to ensure the transmit power. As the operating frequency increases, high integration becomes increasingly important. Obviously, a small wavelength of THz is very beneficial for implementing a large-scale antenna array with a small size. But the small wavelength also poses corresponding challenges.

Up to now, much progress has been made in key technological breakthroughs and prototype system development for THz communication and sensing systems. For example, Zhejiang University developed a multi-channel THz wireless communication system based on photoelectric combination [12]. The system uses an eight-channel THz carrier for modulation to achieve ultra-high-speed wireless communication, which is with a working frequency of 0.4 THz, a modulation method of 16QAM, and a transmission rate of 160 Gbit/s. The advantage of the system lies in achieving ultra-high transmission rate and improving bandwidth utilization. In 2020, the University of Electronic Science and Technology of China achieved THz high-speed wireless communication with a working frequency of 0.22 THz, a communication distance of more than 1000 m, a bit error rate of less than 1E-6, and a transmission rate of more than 20 Gbit/s [13]. For the sensing technologies, terahertz time-domain spectroscopy (THz-TDS) has been used for material's characterization and process control [14].

This article is organized as follows. After stating the latest progress on THz spectrum and potential application scenarios in Section 2, we discuss THz channel propagation and our latest measurement and modeling results on the THz band in Section 3. In Section 4, we focus on the key components and intermediate radio frequency (IRF) architecture, including THz components and chips, THz antennas and THz integration technologies. The prototypes and measurement results of THz high throughput communication and high precision sensing system will be depicted in Section 5. It includes the prototype description, measurement environment and configurations, and the measurement results. Finally, we offer some conclusions and suggestions for future research in Section 6.

2 THz Spectrum and Application Scenarios

THz spectrum usually refers to the frequency bands between 0.1 THz to 10 THz with a corresponding wavelength of 0.03 mm to 3 mm, and lies somewhere between microwaves and optical waves, as illustrated in Figure 1. Due to its unique position in the EM spectrum, THz has the characteristics of microwaves, such as penetration and absorption, as well as the spectral resolution of optical waves.

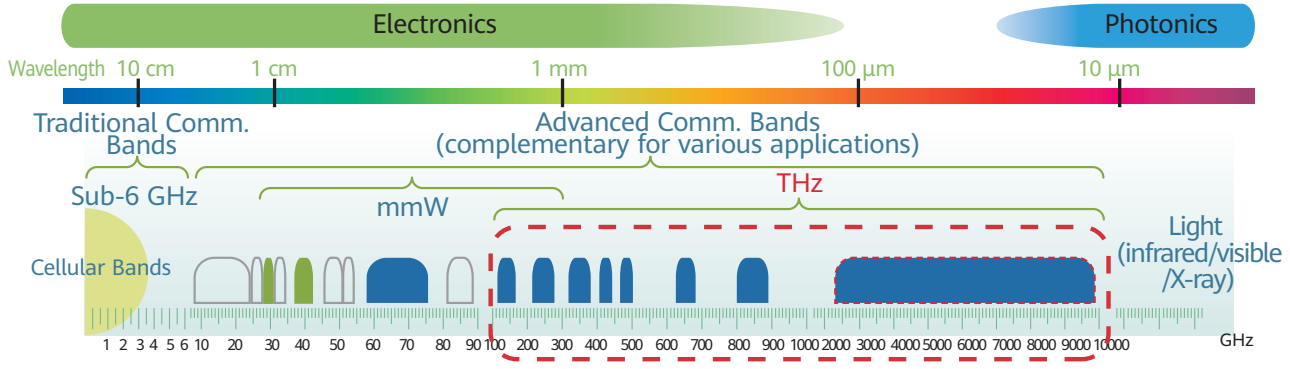

Figure 1 Position of THz waves in the radio spectrum

For a long time, THz spectrum is described as the last virgin land of the radio spectrum. Only a few scientific and astronomical services are deployed in these frequency bands, especially in bands above 275 GHz. In spite of having abundant spectrum and supporting a high transmission rate and strong anti-interference, there are still many practical technical limitations.

However, this has partially changed with the development of integrated components and circuits, and the emergence of various services that require ultra-high data rate transmission. At the World Radio Communication Conference 2019 (WRC-19) [15], RR No. 5.564A was approved, and four globally harmonized frequency bands with a total bandwidth of 137 GHz (i.e., 275–296 GHz, 306–313 GHz, 318–333 GHz, and 356–450 GHz) were allocated for the implementation of land mobile and fixed service application in the frequency range of 275 GHz to 450 GHz, on the basis of study outcomes of Agenda Item 1.15 (WRC-19). Therefore, with the addition of the spectrum allocated at the previous WRCs, there are more than 230 GHz Mobile Service spectrums. Table 1 describes the allocated mobile frequency bands with a contiguous bandwidth greater than 5 GHz.

Table 1 Allocated frequency bands of mobile service in the frequency range of 100–450 GHz

Frequency (GHz)	Contiguous Bandwidth (GHz)
102–109.5	7.5
141–148.5	7.5
151.5–164	12.5
167–174.8	7.8
191.8–200	8.2
209–226	17
252–275	23
275–296*	21
306–313*	7
318–333*	15
356–450*	94

* Allocated for Fixed Service/Mobile Service at WRC-19, 2019.

Such abundant spectrum reserves will drive the rapid development of the THz communication technologies. First of all, it can facilitate extremely high-data-rate connection of the existing wireless transmission applications, such as fixed wireless access (FWA), wireless cellular front-hauling and backhauling, and some short-range link communications [16]. It can increase their connection rates from tens of Mbit/s or several Gbit/s to the unpredictable hundreds of Mbit/s or even several Tbit/s, which is truly comparable to the connection experiences of optical fibers.

Furthermore, the ultra-fine beam generated by the ultra-large-scale antenna array can be implemented in the THz frequency band, which makes high-precision positioning and high-resolution sensing possible. This will support the emergence of new services that are beyond just communication. Shorter wavelengths imply smaller antennas, so small devices can be packed with tens or hundreds of antennas, which are beneficial for angle estimation. The gesture recognition on smartphones is a good example. From the perspective of the base station side, enabling the sensing/imaging feature in future International Mobile Telecommunications (IMT) systems are also important application scenarios for supporting external environment recognition and map reconstruction in THz communications [6].

3 THz Channel Propagation and Modeling

Propagation channel modeling is a fundamental part of wireless communications. Historically, the stochastic channel modeling methodology has dominated the wireless communication channel model. The stochastic channel model can describe the propagation channel using simple

statistical parameters with a low computational complexity of implementation. Many projects and standards, such as 3GPP-SCM, WINNER-I/II, COST2100, and MESTIS, belong to this family. In 2015, the 3GPP 38.901 has released the spatial channel model (SCM) from 0.5 GHz to 100 GHz, which become the 5G standard channel model. However, in 6G communication, the spectrum requirement has extended from millimeter-wave bands to THz bands. In the THz band channel modeling, we will face some new challenges and propagation features which are quite different with millimeter waves.

For the propagation attenuation aspect, THz waves will experience higher path loss than millimeter waves and in some situations the molecular absorption should be considered. In the THz band, the ultra-large bandwidth will result in frequency response inconsistency and higher delay resolution. With frequency increase, the wavelength will decrease to the millimeter level. This implies the wavelength will be comparable with the surface roughness of most of the furniture in the environment, which means the new scattering feature should be modeled. Furthermore, the new small-scale parameters including the delay spread, angular spread, and clusters should be restudied under the stochastic channel model.

Apart from communication, the THz band can be a candidate for sensing applications. In contrast to the communication channel, the sensing channel focuses on different parameters and methodology. For example, the imaging channel requires the deterministic channel coherence of the aperture antenna and the geometry information, and this feature is contradictory to the traditional stochastic channel modeling approach. This means that the stochastic channel models are not suitable for sensing applications, whereas deterministic modeling approaches are favored. However, a single channel modeling scheme may not meet the evaluation requirements of all ISAC applications. For sensing applications such as sensing assisted beamforming, the stochastic modeling can be adopted. However, localization and tracking cases, since description of EM information is not required, the ray tracing can be considered as a strong candidate. On the other hand, imaging and recognition need to take the EM algorithm into account when the sizes of scatterers are approximate to wavelength [17].

Based on the new challenges and requirements, we propose a hybrid channel modeling methodology to support the THz band communication and sensing. Depending on different applications, different approaches are used for channel generation and system-level or link-level evaluation. A few suggested channel modeling methods are listed in Table 2.

Table 2 Terahertz channel modeling methodology

Application	Channel Modeling Method
Communication	Stochastic
Positioning	Stochastic (GBSCM)
Localization and mapping	Ray-based
Imaging and recognition	EM-based

In the next section, we will introduce our current THz band channel measurement campaign progress, and relevant stochastic channel modeling results.

3.1 Channel Measurement System and Measurement Campaign

The THz channel measurement platform consists of a radio frequency (RF) front-end with horn antennas at both transmitter and receiver sides, and a vector network analyzer (VNA). The intermediate frequency (IF) signal is generated by the VNA and then mixed with the multiplied oscillator signal to the RF band, and finally, emitted/received by a horn antenna. With the wide bandwidth, a higher delay resolution can be achieved. To ensure wide-angle coverage, we use a wide beam width antenna at the transmitter sides. On the receiver side, a high gain antenna is mounted on a mechanical rotator to achieve the angular channel response and complement the high path attenuation at the THz band. The measurement campaigns have been achieved at 140 GHz, 220 GHz, and 280 GHz. The detailed parameters are listed in Table 3.

Table 3 Parameters of the measurement system

Parameter	Value	
Frequency band [GHz]	140	220
Local oscillator [GHz]	10.667	18
Start frequency [GHz]	130	201
End frequency [GHz]	143	209
Bandwidth [GHz]	13	8
Sweeping points	1301	801
Transmitter antenna gain [dBi]	15	10
Receiver antenna gain [dBi]	25	25
Azimuth rotation range [degree]	[0:10:360]	[0:10:360]
Elevation rotation range [degree]	[-20:10:20]	[-20:10:20]
Delay resolution [ps]	76.9	125
Maximum excess delay [ns]	100	100

We carry out the channel measurement in a typical meeting room and open office area. The realistic environment can be seen in Figure 2. In the meeting room with an area of 10.15 m x 7.9 m and a ceiling height of 4 m. A 4.8 m x 1.9 m desk with a height of 0.77 m is placed in the center, and some chairs are around the desk. The dimension of the office room in our channel measurement campaign is 30 m x 20 m, including a hallway and an office area. The furniture in the environment includes desks, chairs, tiny plants, screens, etc.

Figure 2 Meeting room (left) and open office (right)

3.2 THz Channel Characterization and Analysis

Path loss is a large-scale fading which reveals the signal power level of the receiver at different places. We evaluate the multi-frequency alpha-beta-gamma (ABG) path loss model for all the measurement sets. As we know, the multi-frequency path loss models cover the relationship between path loss and both distance and frequencies. As a widely used multi-frequency path loss model, ABG model is obtained by adding a frequency-dependent optimization parameter to the alpha-beta (AB) model used in 3GPP. The ABG model can be expressed as

$$PL^{ABG}[dB] = 10\alpha log_{10}\left(\frac{d}{d_0}\right) + \beta + 10\gamma log_{10}\left(\frac{f}{f_0}\right) + X_{\sigma}^{ABG} \quad (1)$$

Where f and f_0 denote the carrier frequency and the reference frequency in gigahertz, respectively. d and d_0 represent the distance between the transmitter and receiver and reference distance. X_{σ}^{ABG} is a zero-mean Gaussian random variable with standard deviation σ_{SF}^{ABG} in dB, which represents the fluctuation caused by shadow fading. In addition, we can see from formula (1) that α and γ represent the dependence of path loss on distance d and frequency f, respectively, while β is an offset parameter.

Based on the measurement campaign, in the meeting room environment, the ABG path loss results on 140 GHz, 220 GHz, and 280 GHz bands are depicted in Figure 3. The proposed ABG path loss model is as follows:

$$PL^{ABG}[dB] = 20.7log_{10}\left(\frac{d}{d_0}\right) + 26.72 + 22.2log_{10}\left(\frac{f}{f_0}\right) + 2.53 \quad (2)$$

More measurement campaign and modeling results can be referred to in literature [18–20].

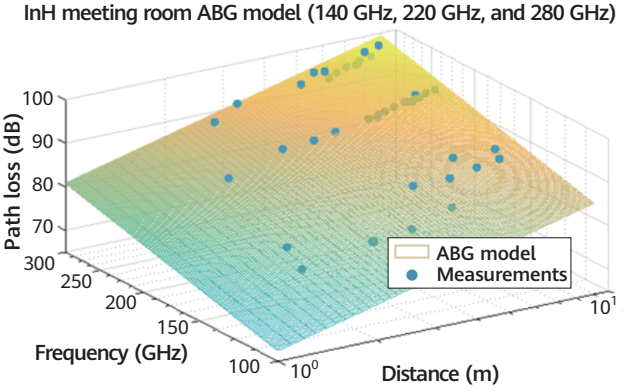

Figure 3 ABG path loss model results at the meeting room

On the small-scale aspect, the THz channel also exhibits different propagation characteristics from the millimeter wave channel. The rough surfaces at the THz band need to be considered carefully as the THz wavelength is comparable to the roughness of object surfaces. The measurements indicate that in the 140 GHz band, multipath components are still rich in the open office due to the abundant furniture. For further study, we choose one receiver position (shown in Figure 4) as an example to analyze the spatial angle of arrival (AoA). We can observe that it is an obviously sparse propagation channel, in which 3 clusters are extracted with 30 dB cutoff threshold. Furthermore, we use the ray tracing mechanism to map the clusters into the geometry space environment in Figure 4b. The propagation paths perfectly match with the geometry map and measurement results. The transmitter antenna beam width is about 30° to cover the entire area. The north direction (upwards direction on the 2D map) is defined as the zero degrees with clock-wise rotation. Based on the geometry reconstruction, from the receiver point of view, the direct path is traced between the TX and RX lines with 8.7° AoA. The second path is coming from the rear left reflected by a monitor screen, and the AoA is –160°. The third path is also a reflection path provided by the rear right monitor screen, and the AoA is 135°. There is at least 90° separation among the three paths. This implies that there are three orthogonal spatial channel streams we can utilize for beamforming design, which is good for beam management and single-user multiple-input multiple-output (SU-MIMO) performance [1].

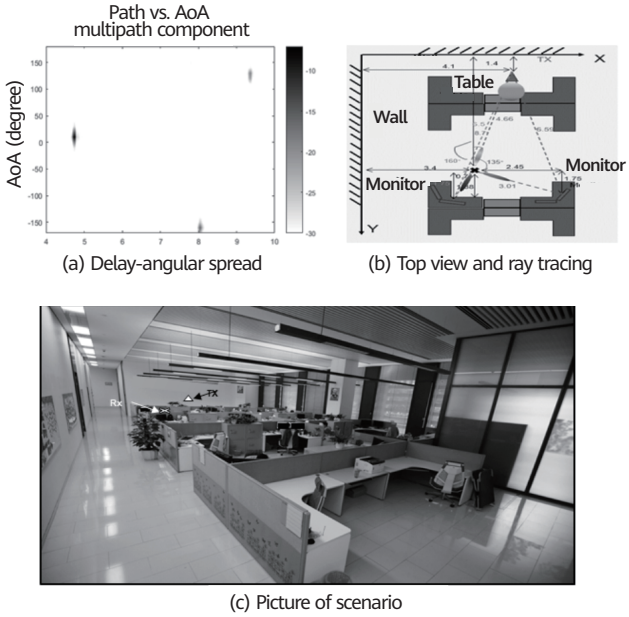

(a) Delay-angular spread (b) Top view and ray tracing

(c) Picture of scenario

Figure 4 Indoor hotspot cell (InH) meeting room 140 GHz measurement scenario

To investigate the penetration characteristic of the THz band, we measure 14 different typical materials to study the penetration loss. Three penetration loss types classified based on the analysis results are presented in Table 4. The THz wave can penetrate the carton and cotton coat easily with only several dB, even transparently. This tells us that the THz wave can be used for safety detection application, such as detecting a knife hidden in the pocket. The second category is the typical outdoor-to-indoor (O2I) material, like the single layer glass, and wooden door. The THz wave shows above 10 dB penetration loss which significantly affects the coverage and capacity. The third category we presented is the ultra-high loss for THz waves. This kind of material contains conductive molecules that severely obstruct THz wave propagation.

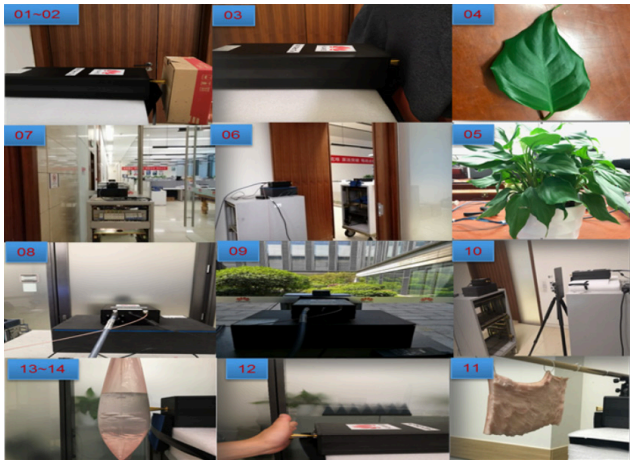

Figure 5 Penetration loss measurement for typical materials

Table 4 Penetration loss of different materials at 140 GHz

Index	Material	Blockage Thickness	Object-Antenna Distance	Penetration Loss (dB)	Loss Model
01	Single -layer carton	2.4 cm	0 cm	2.8	Low loss
02	Double-layer carton	5 cm	0 cm	3.6	
03	Coat	5 mm	0 cm	0	
04	Single leaf	0.5 mm	0 cm	10.6	Middle loss
05	Small indoor vegetation	25 cm	0 cm	29.6	
06	Wooden door	7 cm	50 cm	19.4	
07	Double -layer glass	1.3 cm	50 cm	15.7	
08	Frosted glass	0.6 cm	50 cm	15.2	
09	Double silver low-E tempered glass	1.8 cm	50 cm	55	High loss
10	Metal	3 mm	50 cm	49.6	
11	Pigskin	1.5 cm	10 cm	59	
12	Hand	2 cm	0 cm	59.1	
13	Water	4 cm	0 cm	53.2	
14	Water	7 cm	0 cm	58.4	

A hybrid channel modeling methodology is proposed for the THz communication and sensing. We achieve the THz band sounding system and typical indoor measurement. The SCM-based path loss and multipath components are presented. Based on the analysis results, the THz band shows sparse spatial clustering propagation channel characteristics and sensing capability. In future work, we will investigate the outdoor propagation features for THz band communication and sensing.

4 THz Hardware and Components

In order to meet the requirements of diversified application scenarios in future 6G, it is also necessary to gradually realize the industrialization of THz components and key technologies, so as to realize the large-scale commercialization of the THz communication and sensing

systems. The key THz components, THz antenna, intelligent surfaces, and integration technologies are investigated here.

4.1 THz Components

The "THz gap" is due to the lack of compact source and detector technology. So highly pure THz sources, high gain and high power amplifier that operate at the THz band and the highly sensitive THz receivers are key technologies that enable THz applications. What's exciting is that the silicon-based THz components and system have shown a continuing growth in sensing, imaging and communication applications beyond 100 GHz. In addition, by integrating III-V material and device on silicon, the system performance can further be leveraged beyond 500 GHz. Both silicon microelectronic and photonic devices [21] can benefit from this integration approach. The different technologies available to build THz and sub-THz sources are shown in Figure 6.

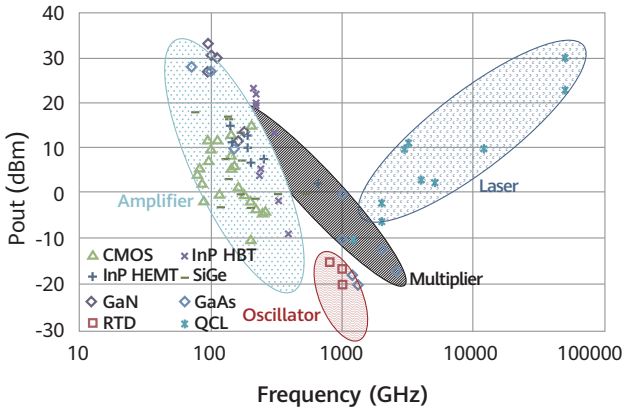

Figure 6 Terahertz gap with respect to source technology

The maximum oscillation frequency f_{max} of transistors determines the speed of the system. The demand of higher density electronics and faster system performance drives higher CMOS scaling, i.e., higher f_{max}. In conventional CMOS and BiCMOS technology, the f_{max} of a transistor is between 200 GHz and 350 GHz, i.e., 45–65 nm nodes [1]. With SiGe BiCMOS technology, the transistor can reach f_{max} of 0.5 THz, i.e., 130 nm node [1]. Beyond f_{max}, the CMOS performance degrades with device scaling. Although nonlinear effects of the device may be exploited to generate harmonic power and detect signals, the efficiency is low. III-V compound semiconductors can drive the f_{max} far beyond 0.5 THz. InP-based HEMTs can reach f_{max} of 1.5 THz [22] and double heterojunction bipolar transistors (DHBTs) can bring the f_{max} up to 1.15 THz [23]. Another example is GaN HEMTs ($f_{max} \approx$ 0.58 THz [24]).

Frequency multiplication and higher harmonic extraction from on-chip oscillators are two common ways to generate THz signals. At the THz band, the planar Schottky diode technology plays a crucial role, and at room temperature, demonstrates powers of 100 µW at 1.2 THz, 15–20 µW at 1.5–1.6 THz, and 3 µW at 1.9 THz. [25–26] provided a comparison of state-of-the-art THz sources in CMOS and SiGe technologies. Sources with both conducted and radiated power were discussed and compared. Due to the parasitic effects at the THz frequency, it is preferred that antennas are integrated on chip to simplify the packing process and prevent unnecessary signal losses. Equivalent isotropically radiated power (EIRP), defined as the product of the radiated power and directivity of the antenna radiation pattern, is used to characterize this type of THz sources. It was shown that by utilizing the power combining technique, the radiating antenna array can significantly increase the output power [27], which is essential for THz beamforming and beam steering application. In a resonant tunneling diode (RTD) oscillator, the on-chip antenna is also directly decoupled for the signal-coupled output, and fundamental oscillation up to 1.98 THz and output power of 0.7 mW at 1 THz by a large-scale array have been reported [28].

Amplification of weak THz signals is a very important function in the system. An effective THz amplifier operates approximately 1/2 of the transistor's f_{max} and can reach 2/3 of f_{max} with proper design [29]. Currently, amplifiers using the advanced 35 nm InP HEMT process have achieved 1.1 THz signal amplification. The power amplifiers monolithic microwave integrated circuit (MMIC) designed with the InP DHBT process can output 220 mW power at 220 GHz [30]. Using the three-dimensional (3D) additive fabrication process, a 16-way solid state power amplifier module reaches 820 mW output at 210 GHz, making low-end THz applications possible. Figure 7 demonstrates a GaN HEMT power amplifier and its package operation at 220 GHz. The saturation output power reaches 18 dBm. Compared to the III-V counterpart, the output power and operation frequency of CMOS amplifiers are much lower. The best amplification application for CMOS is at 140 GHz, and the gain can be achieved at 200–300 GHz using positive feedback technology [31]. BiCMOS currently operates at a maximum amplification frequency of 310 GHz, achieving 4 dBm of output power [29].

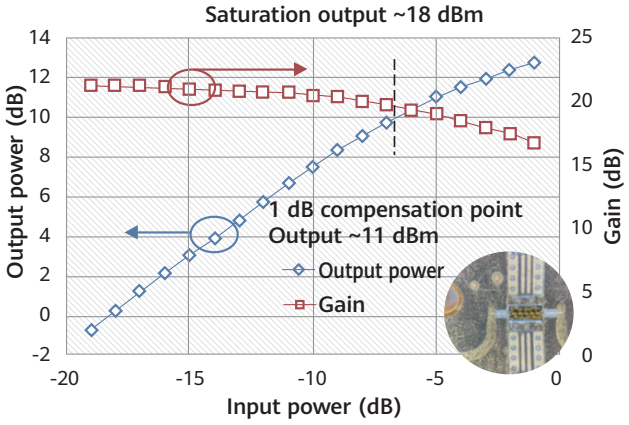

Figure 7 Output performance of 220 GHz GaN HEMT power amplifier

THz receivers can be classified as heterodyne and direct detector receivers. A heterodyne receiver down-converts the THz signal to an IF frequency driven by a local oscillator and it can acquire both phase and amplitude information from the THz radiation, i.e., coherent detection. [1, 26] discussed a variety of THz receivers based on both silicon and III-V technologies, ranging from 200 GHz up to near 1 THz. It showed that InP-based receiver can offer similar (below 300 GHz) or better (beyond 500 GHz) performance in terms of gain and noise figure in general. Coherent receiver has been demonstrated in both THz imaging and communication applications [32].

However, practical implementation of high density 2D on-chip antenna array remains challenging due to the system complexity and high power consumption. Moreover, multiport receiver technology is a desired feature to enable multifunction and multimode THz communication and imaging and sensing application. In [33], multiport receiver technology was reviewed and different multiport architectures were discussed. A 6-port receiver system based on multiport interferometer technique was detailed which is capable of handling AoA detection as well as data communication. This architecture can potentially find its application in future THz joint radar-communication, simultaneous localization and mapping, and imaging/sensing systems.

On the other hand, a direct detector can convert the illuminated THz radiation power to a measurable DC current. The receiver system usually consists of a CMOS integrated field-effect transistor (FET) or SBD with simple antennas such as loop or patches coupled to it and a readout circuitry that rectifies the impinging THz radiation power to a readable DC current. In [1], comparisons of state-of-the-art direct receivers were provided. It showed that direct receivers in general have higher noise power compared to their heterodyne counterparts and are therefore mostly used in THz imaging and sensing application. Direct receivers can better integrate with silicon in large numbers/pixels due to their simple architecture and low power consumption. They have been widely used in THz camera devices when packaged into focal-plane array configuration [34]. The different technologies available to build THz and sub-THz receivers are shown in Figure 8.

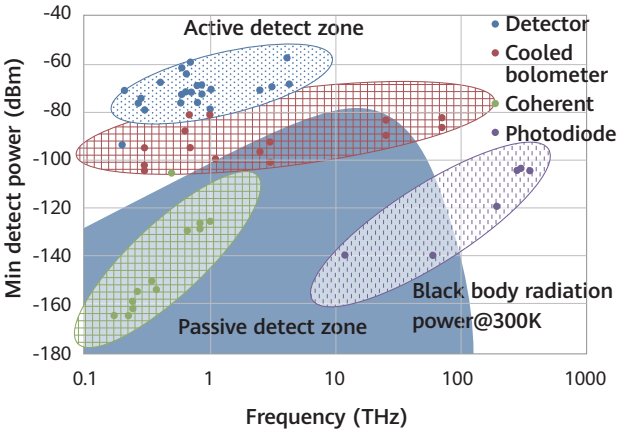

Figure 8 Terahertz receivers with respect to source technology, with 1 Hz resolution bandwidth (RBW)

4.2 THz Antenna

THz "tile-able" array is attractive as it allows for high radiated power by beam manipulations from large-scale THz antenna arrays. In a THz "tile-able" array, large number of antennas are integrated on chip to ensure the structural compactness and high power efficiency to prevent unwanted parasitic loss. In this case, the EIRP is used to indicate the effective output power of the THz source, which combines both the radiated power and directivity of array. High-level integration and scalability are two important considerations in tile design, and smartly using existing on-chip structures has become a promising approach. In [35], a fully "tile-able" array was proposed that uses an existing on-chip slot mesh structure in multiple functional ways, so a high radiated power of 80 μW was achieved. Such structural multi-functionality was further leveraged in [36], in which a de-centralized architecture was proposed and the scale is pushed to be comparable with that of direct detector arrays, however with an approximately 4300x sensitivity improvement. In [37], a densely integrated and unified paralleled amplifier and antenna architecture

was demonstrated. A patch antenna with co-existing topologically paralleled transistors was designed, and it can perform power radiation and amplification simultaneously. The concept was then validated using a standard 65-nm CMOS process. A set of chips were fabricated at 146 GHz and the compact unified prototypes showed an amplified radiation with 3.4 dB gain enhancement through a single element and 6 dB gain enhancement through 2×2 layout. It is also noted that frequency tuning can be achieved by varying bias.

Programmability is another desired feature of THz "tile-able" array. Limited configurability has been demonstrated mainly through electrically, mechanically, or thermally controlled reconfigurable materials [38–39]. The ultimate programmability is one that can configure the transmitted THz fields digitally and receive the THz fields with arbitrary specification. This not only includes beams synthetization with desired characteristics through beam steering or beamforming to enhance the radio performance, but also includes beam with "pixelated" or "voxelated" configuration to form a desired image or video at the user end. In addition, CMOS integration is an important consideration to allow for low-cost fabrication. [40] proposed a THz sensing surface with a log-periodic antenna loaded with 16 distributed detectors. By changing the detector capacitance bank configurations, the antenna is reconfigured to different working states. The system was fabricated with a standard 65 nm CMOS process and tested from a wide frequency range from 0.1–1 THz with responsivity to different angles of direction and polarization. [41] demonstrated a dynamically programmable array made of split-ring resonators loaded with 8 switches fabricated using a 65 nm CMOS process. 256 states (8 bits) were reported combining both amplitude and phase control. The coded surface was shown to project simple letter holography using measured near fields. Though the image resolution is low, this field projection provides a powerful approach for many applications such as sensing, qualitative imaging, and beamforming/beam steering with a silicon compatible approach.

4.3 Intelligent Surface

Signal deterioration is one of the major issues in THz communication. The high propagation loss at the THz band results in a very short communication distance. The signal blockage and misalignment impacts are more severe at the THz band. This can affect the THz network coverage and number of user accesses. Moreover, the multipath environment can cause the signal to be "null" at some locations. Therefore, an intelligent wireless system capable of adapting to a time-varying wireless environment is needed to meet these challenges.

Programmable surface is one promising candidate to provide an intelligent and controllable wireless communication system. When applied on the surface of various objects,

such as buildings, it can realize various functions such as beamforming and polarization control and provide seamless connections.

In [42], intelligent surface is classified into passive surface (also termed as reconfigurable intelligent surface, RIS) and active surface (also termed as large intelligent surface, LIS). The passive RIS performs some basic functions such as beam reflection, collimation, and polarization. It operates in an energy-efficient way since it is usually composed of low-cost passive components that are self-power-sustaining. The active LIS, on the other hand, performs the RF role partially or fully. It is therefore usually equipped with some RF circuitry and signal processing unit which can be power-consuming. In addition to the basic beam manipulation, active LIS can further amplify the impinging wave, synthesize the desired beam pattern and perform simple signal processing function. Intrinsically, both passive and active intelligent surfaces are made of reconfigurable radiators or scatterers. These radiators can be made of reconfigurable material, such as phase changing material or liquid crystal, or they can be controlled through a programmable interface. Either way, they enable the surface to perform in an "intelligent" way in response to the time-varying wireless communication environment.

From the microscopic perspective, the radiator element can be of simple antenna geometry, such as loop, patch, and wire. By loading the antenna with different passive components, such as varactor diodes, through a digital controller, the working states of antenna can be changed, and therefore its beam pattern can be steerable. In [43], a loop antenna loaded with 8 small extra loops was designed as the radiator element. Each small loop can be digitally controlled with two states ON and OFF, and therefore 8-bit control can be realized through a programmable interface. A chip tiled with 576 such elements was fabricated which provided both amplitude and phase control, dynamic beamforming and multi-beam formation at 0.3 THz. It was also demonstrated that the surface can project simple holographic letter images qualitatively.

Figure 9a shows a wireless communication environment enabled by intelligent surfaces. When installed on the exterior of buildings, intelligent surfaces can be used to create connections between buildings, vehicles, or automated guided vehicles (AGVs) in cases where there is no direct link between them or the link is blocked by obstacles. Intelligent surfaces can further extend the radio coverage from outdoor base stations to indoor users. By programming their working states, intelligent surfaces can perform beamforming and direct its beams to the target end users dynamically and relay information to the desired locations with attenuation compensation. Beamforming from intelligent surfaces can also help transfer power to Internet of Things (IoT) devices and sensors.

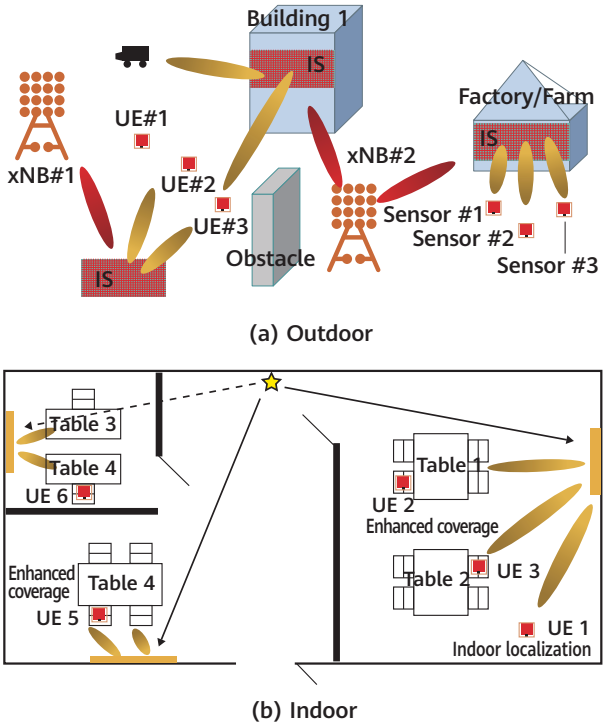

Figure 9 Typical RIS use cases for THz

When deployed in an indoor environment as shown in Figure 9b, e.g., attached to a wall, intelligent surface can help direct the signal to the target user locations where the signal experiences multipath fading and path loss due to wall blocking and scattering from furniture, plants, etc. Intelligent surfaces can also be used for high precision indoor localization as its large surface aperture can help increase location precision.

In another embodiment, the scattering elements can be of high-dielectric-index nanopillars or nanofins. Each element is modified geometrically to manipulate the amplitude, phase, and polarization of the incident EM wave. In [44], the working mechanism underlying this type of metasurface was discussed. The phase modulation of the transmitted wave is due to different propagation constant of the nanopillars. For example, the induced geometric phase can occur in crossed polarized light linearly with respect to the

orientation angle of the nano-element [44]. This provides a possibility for optical holography application. [45–46] demonstrated that this all-dielectric metasurface can be used to encode the hologram by using unit element with varying orientations. Both amplitude and phase information can be recorded and controlled independently. Then, by collecting the transmitted light at the image plane, the original object can be faithfully reconstructed pixel by pixel using a standard computer-generated hologram algorithm.

Though the optical metasurface shows its ability in holography application with high fidelity image reconstruction, these surfaces are static after fabrication. A dynamic control of the holograms is desired to achieve a true holographic display. Although the concept of programmable metasurface and reconfigurable material such as phase changing material can be applied here similarly, it is still very challenging to configure pixel level wavefront representation that can reflect both phase and amplitude information of the original object dynamically in the visible spectrum. Multiplexed metasurface is another way to address this problem. There are various multiplexing methods. Wavelength division multiplexing [47–48] uses nanostructures that are multiplexed in a subwavelength scale and capable of manipulating wavefronts of multiple frequencies. Angle and polarization multiplexing can respond to light of different angles of incidence and polarization. In [49], an orbital angular momentum (OAM) holographic metasurface capable of reconstructing a range of OAM-dependent holographic images was demonstrated using a single meta-hologram with high spatial-resolution. It showed that incident OAM beams of 4 different modes can independently reconstruct distinctive holographic images of alphabet letters from the same multiplexed OAM meta-hologram. Recently, [50] demonstrated a space-multiplexed metasurface that can achieve 2^{28} different holographic frame/image at a maximum rate of 9523 frames per second. In [50], the entire metasurface is divided into many different sub-regions which are combined at different times in a specified configuration modulated by a high-speed dynamic structured laser beam modulation module to project images like an electronic meter. Strings containing digits (0 to 9) and letters can be fully reconstructed and displayed in a meaningful way using this approach.

4.4 Integration Technologies

A crucial element in THz system is the packaging and integration technology. The most important parameters are losses and reflections in the chip-to-substrate transition. At present, the commonly used metal module package has lower integration level, and higher cost. It will be replaced by high-density integrated technologies in the future. Multichip module (MCM), system-in-package (SiP), and heterogeneous integration are promising candidates. MCMs built on high temperature co-fired ceramic (HTCC) or low temperature co-fired ceramic (LTCC) substrates have been used in THz packages. Antenna and silicon lenses are integrated in the package to reduce connection loss and enhance system EIRP [51]. The through-silicon via (TSV) process has better integration and process precision and can be used at higher frequencies [52]. The embedded wafer level ball grid array (eWLB) technology usually used at low frequency (with interposer or distribution layers) can also be used in lower end of THz [53] as SiP technology.

Silicon-based integrated circuits (ICs) prevail due to their low cost and high level of on-chip integration; III–V compound semiconductors represented by GaAs and GaN can provide a higher transmission power. A heterogeneous integration platform can provide better performance, e.g., higher output power, while still retaining the silicon's advantage. Wafer-level integration using Benzocyclobutene (BCB) provides a 2D integration method [54]. The alternative approach bonds the wafer or die of III-V materials onto a patterned silicon wafer, for instance, a 3D BCB-based wafer bonding integration scheme or wafer-scale low-temperature oxide-to-oxide bonding [55]. These methods seem promising as they retain the silicon's advantages while leveraging the high power and high frequency operation ability of III-V semiconductor.

5 THz System and Testing

In this section, our contributions on THz communication and sensing systems are described in detail, which includes link simulations, testing and result analysis of THz communication and sensing systems and prototypes.

5.1 THz Communication System

Recent technology progress in electronic, photonic and material technologies are closing the gap in THz transceiver design. Consequently, THz signal generation, modulation, and radiation methods are converging, and corresponding channel model, noise cancellation, and hardware-impairment compensation and ultra-wideband signal processing techniques for wireless communications are also emerging.

As shown in Figure 10, there are so many significant technical differences between normal frequencies and the THz band as result of channel propagation characteristics, e.g., large atmospheric propagation loss, strong directivity, and ultra-narrow beams. They limit signal coverage and mobile access. The impairment characteristics of broadband RF device, e.g., strong phase noise, frequency selective memory in-phase and quadrature-phase imbalance (IQI) and in-band flatness, require ingenious algorithm design, and ultra-wide bandwidth requires an ultra-high speed analog-to-digital converter (ADC)/digital-to-analog converter (DAC) conversion rate. So from baseband to RF, the design of a complete THz communication system is faced with great technical challenges.

As mentioned previously, it is valuable to explore novel signal processing architectures, waveform design, and corresponding compensation algorithms to solve the challenges of Ultra-High Frequency and Ultra-Wideband.

Up to now, because of the absence of experimental platforms for true THz communications, the majority of THz-band communication works are mainly theoretical and limited experimental validation. In this paper, our THz communication platform, i.e., the integrated testbed for ultra-broadband wireless communications at 220 GHz frequency, is presented, and the block diagram of the testbed is illustrated in Figure 11. As shown, advanced spatial and polarization multiplexing technologies are used to improve spectral efficiency.

The THz communication system consists of an RF transmitter and an RF receiver. At the transmitter, the data bits are organized in frames, modulated into symbols, undergo pre-equalization, pulse shaping, fractional delay pre-compensation, and digital IF modulation, and are fed to the high-speed DAC board. Then analog signal with a center frequency of 12.5 GHz is output. Analog IF signal is connected with the THz analog Front End.

At the receiver, the well-designed digital baseband physical algorithm is employed, the received THz signals from analog front end are digitized by the high-speed ADC boards which are synchronized, and undergo channel estimation and equalization, phase noise estimation and cancellation, interference cancellation, nonlinearity compensation, demodulation and decoding.

Field trial experiment was conducted with 2 × 2 polarization-MIMO. The field trial experiment was conducted at Chengdu, China. The TX/RX link distance is 330 m from the rooftop to the ground, and the channel is almost line-of-sight as shown in Figure 12 [56].

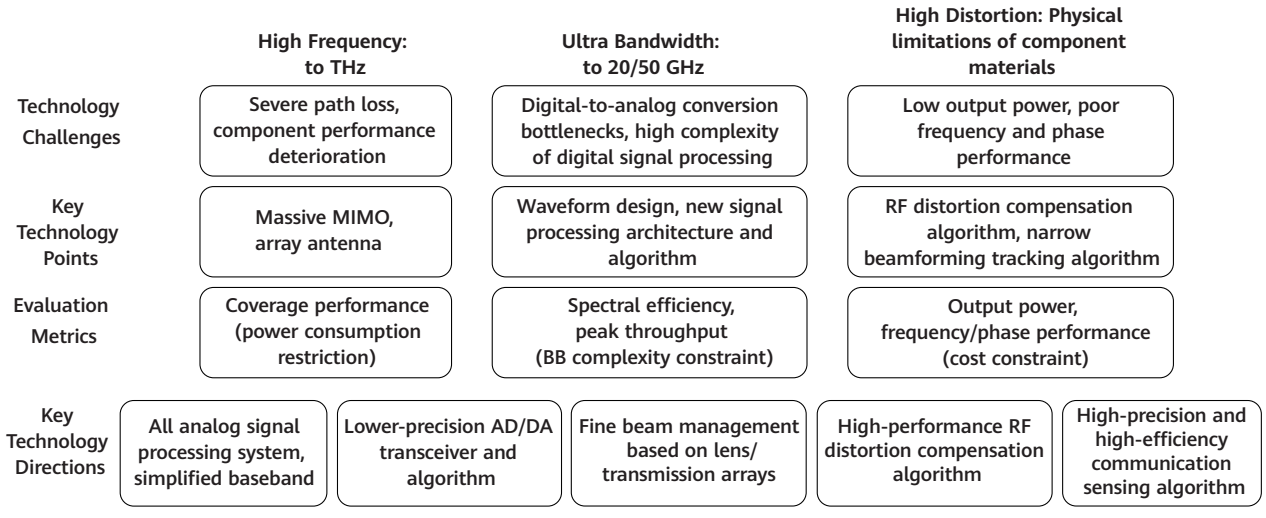

Figure 10 THz communication technical challenges

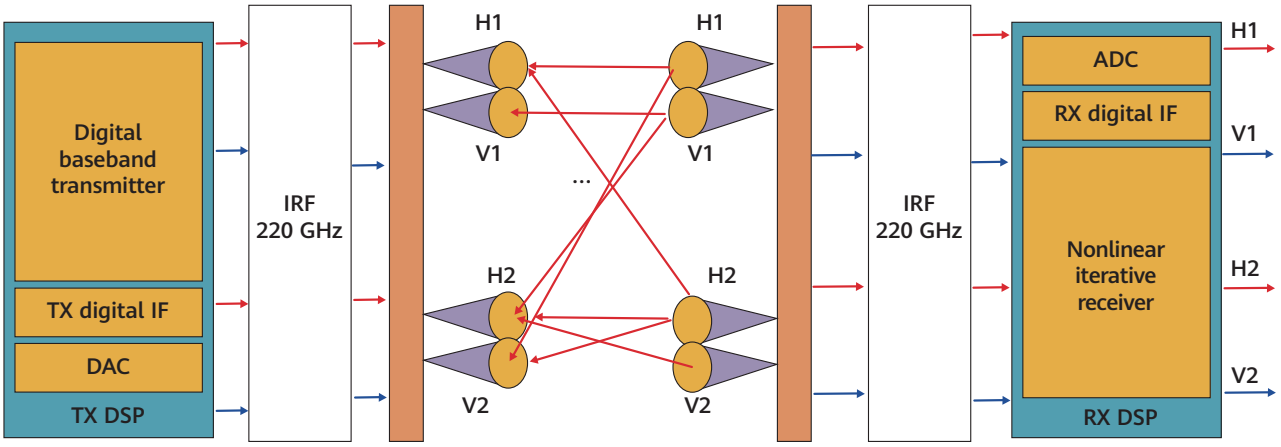

Figure 11 THz communication testbed system architecture

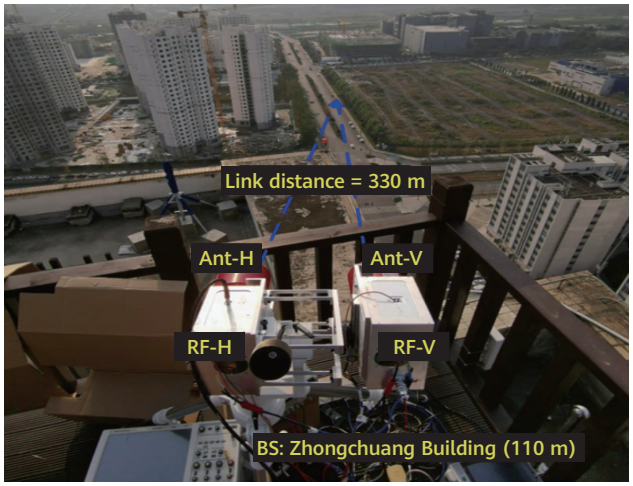

Figure 12 THz field trial, 2 × 2 polarization-MIMO system

In order to compensate the constant frequency selective response of the THz RF components, a digital pre-equalization (DPEQ) filter at the transmitter is implemented. The frequency response H(k) is calculated by comparing the IF signals transmitted and received within the bandwidth of the system components:

$$H(k) = \left(\frac{P_r(k) - P_n}{P_s(k)}\right)^{1/2} \quad (3)$$

Where $P_r(K)$ is the received signal power with noise at the kth frequency, $P_s(K)$ is the transmitted signal power, and P_n is the noise power for the whole observation bandwidth.

We theoretically and experimentally tested a time-domain DPEQ scheme for wide-bandwidth THz communication systems, which is based on the feedback of channel characteristics from the receiver-side blind and adaptive equalizers. Based on the proposed DPEQ scheme, we theoretically and experimentally studied its performance in terms of various channel conditions as well as resolutions for channel estimation. Besides, the significant improvement in channel flatness and mean squared error (MSE) performances were also demonstrated.

The channel frequency response curve is shown in Figure 13, indicating that the flatness in the signal band is irregularly fluctuating with about 16 dB maximum fluctuation in 12 GHz bandwidth. When pre-equalization is enabled, the flatness is compensated and performance improvement is noticeable.

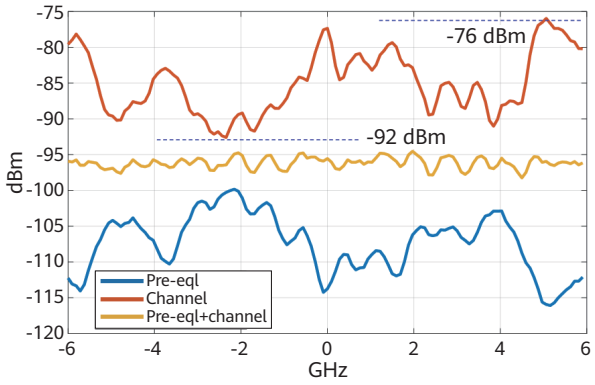

Figure 13 Channel and pre-equalization power spectral density (PSD)

The corresponding demodulation constellation is shown in Figure 14. Pre-equalization at the transmitter does not amplify channel noise, and equivalent signal-to-noise ratio (SNR) is improved. Therefore, resolution of constellation map is increased even for higher order modulation, e.g., 64QAM.

To maximize spectral efficiency and increase THz link capacity, polarization multiplexing is considered in our prototype. The vertically or horizontally polarized waves mean that the electrical field is oscillating in the vertical or horizontal direction respectively. Two ideal polarized antennas results in two independent channels doubling the capacity of the system.

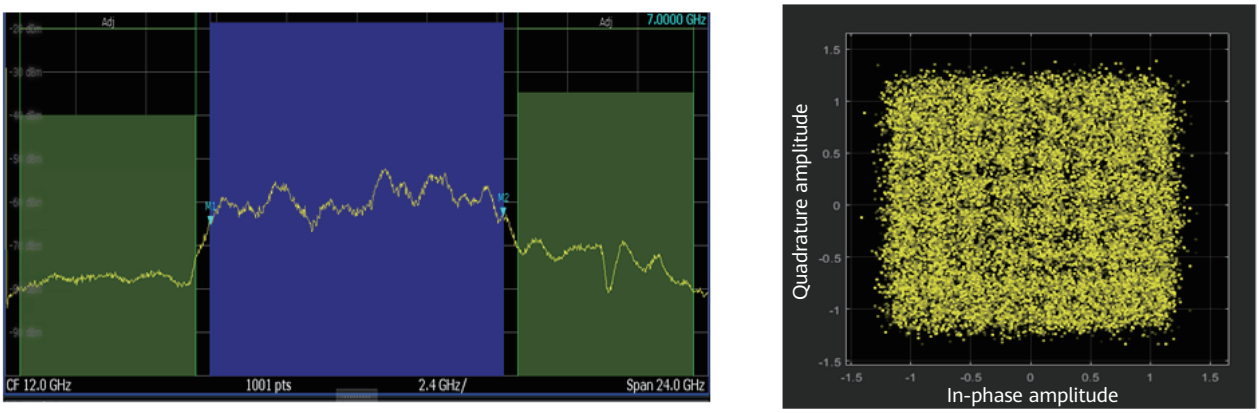

(a) Without pre-equalization

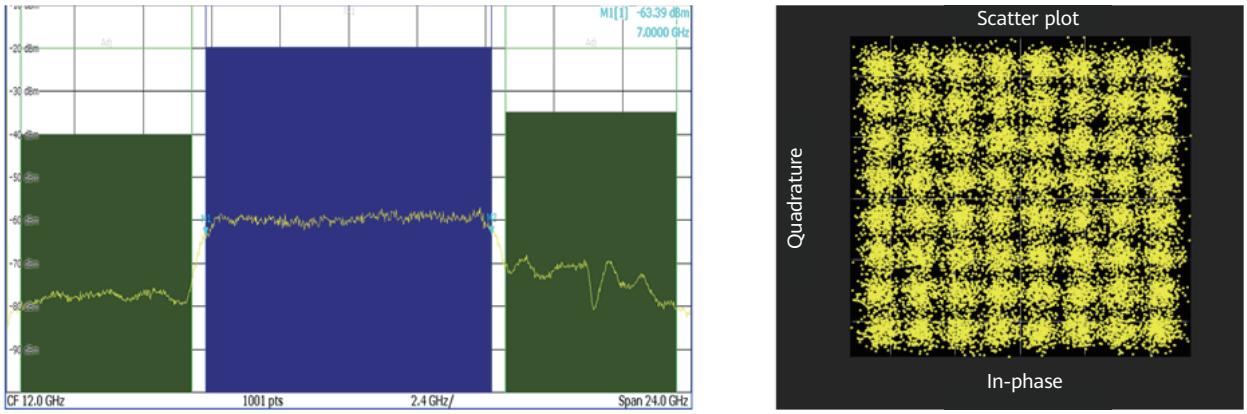

(b) With pre-equalization

Figure 14 PSD and demodulation constellation

However, a real system always experiences imperfections, such as crosstalk between polarizations. The interference between the signals inevitably occurs because of cross-polarization discrimination (XPD) of the antenna and channel degradation. This is because antenna polarization is not ideally isolated. Different polarizations may have different propagation characteristics in different channel scenarios (e.g., under raining environment), resulting in polarization leakage between channels. This leakage can be quantified using the channel XPD factor. It describes how much power from one polarization leaks into another polarization, thus reducing the system's ability to separate between the two polarizations. It is defined for the vertical and horizontal components respectively as [57]

$$XPD_V = \frac{E\{|h_{V,V}|^2\}}{E\{|h_{H,V}|^2\}}, XPD_H = \frac{E\{|h_{H,H}|^2\}}{E\{|h_{V,H}|^2\}} \quad (4)$$

where $h_{V,H}$ is the flat channel impulse response between the vertically polarized transmitter and horizontally polarized receiver with the subscripts V and H representing the vertical and horizontal antennas.

The XPD measurement is shown in Figure 15. The recording operation was performed 10 times during one day to measure the receive powers of two polarizations. The results show that mean XPD is about 19 dB with ±2 dB fluctuation influenced by mechanical deformation and beam misalignment.

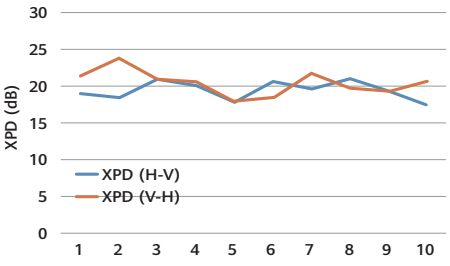

Figure 15 XPD measurement

To eliminate this interference, cross-polarization interference cancellation (XPIC) technology is used to receive signals horizontally and vertically. The signals in the two directions are then processed, and the original signals are recovered from the interfered signals. The assignment of the same frequency to both the vertical and horizontal polarization on a link is allowed.

The consistency of RF components is difficult to achieve since the signal bandwidth is very wide, in-band channel characteristics difference between H polarization and V polarization is significant, and the impairment between the effect of XPD and the frequency selectivity of the channel is coupled. It is necessary to design an ultra-large bandwidth polarization interference cancellation algorithm.

Polarization interference cancellation performance is shown in Figure 16. It can be observed that the contrast convergence curve in time domain is stable, and it has about a 2 dB performance gain.

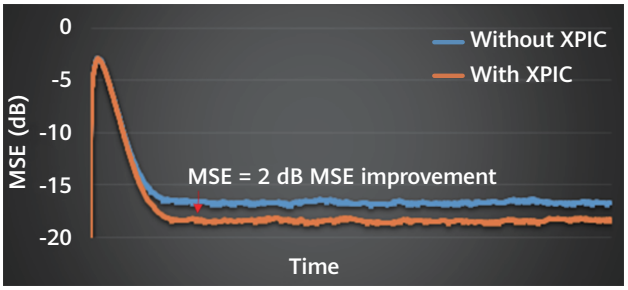

Figure 16 Polarization interference cancellation performance

Classical coherent architectures are combined with high spectral efficiency schemes. This entails numerous constraints on the design of RF components especially at the oscillator level. Indeed, high frequency oscillators severely impair THz systems with phase noise [58].

There are several different methods to model the random process of phase noise, such as the well-known Wiener random process and Gaussian random process. In our design, to model the influence of phase noise, a zero-mean White Gaussian Noise is first generated and then is passed through an infinite impulse response (IIR) filter. After that, the filtered noise is added to the angle component of the input signal. This generation process is shown in Figure 17, in which F_0 is the frequency offset, *phase_noise* is the prescribed phase noise level at the frequency offset F_0 , F_s is the sampling frequency, and K is the gain factor controlling the phase noise level at the frequency offset F_0.

$$\phi(n) = \phi(n-1) + K\boldsymbol{w}(n) \quad (5)$$

The power spectrum of the phase noise $e^{j\phi(n)}$ is equal to

$$P(f) = \frac{1}{F_s} \cdot \frac{1-e^{-K^2}}{1+e^{-K^2}-2e^{-K^2/2}\cos(2\pi\frac{f}{F_s})} \cdot \mathrm{rect}(\frac{f}{F_s}) \quad (6)$$

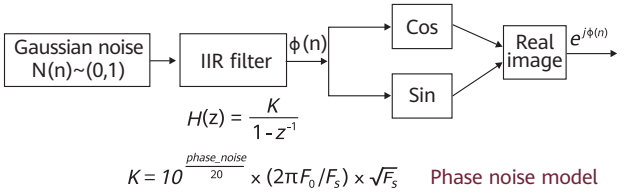

$K = 10^{\frac{phase\_noise}{20}} \times (2\pi F_0/F_s) \times \sqrt{F_s}$ Phase noise model

Figure 17 Phase noise model

Normally, in a multi-channel system, the phase noise at each channel will be independent with each other due to the distributed local oscillator at each channel. It will degrade the system performance, and the new phase estimation and compensation schemes will be involved to solve this problem. A specially constructed pilot code is used to project the mixed phase noise onto the space-time orthogonal code space. The distributed Master and Slave phase-locked loop (MS-PLL) and quasi-linear interpolation phase noise suppression (PNS) algorithms are used to track and compensate the phase noise in the multi-channel signal space dimension, which is a low overhead (< 5% pilot proportion) solution, and is able to effectively suppress typical distributed independent phase noise.

Although THz frequency oscillators have an absolute strong phase noise, a higher symbol rate means a shorter symbol switching time, and a stronger phase noise correlation between consecutive symbols.

As is shown in Figure 18, the powerful MS-PLL architecture can track and compensate for the impact of phase noise greatly. When MS-PLL is enabled, the pilot interval is changed, and the impact is not obvious. Compare pilot interval 16 with 256, the performance gap is not more than 1 dB.

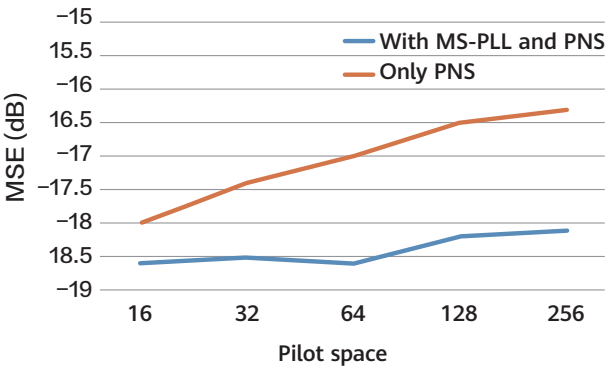

Figure 18 PNS performance

Due to the narrow beam (3 dB beam-width is only 1°), mechanical installation and antennas alignment are particularly important to support sufficient receive power. In Figure 19, the transmit power is 16 dBm, and the antenna gain is 43 dBi. According to the link budget, for a 330 m link distance, the RX antenna ports should receive power of –43.6 dBm. Considering the line loss and atmospheric absorption, the measured receive power is –46.7 dBm.

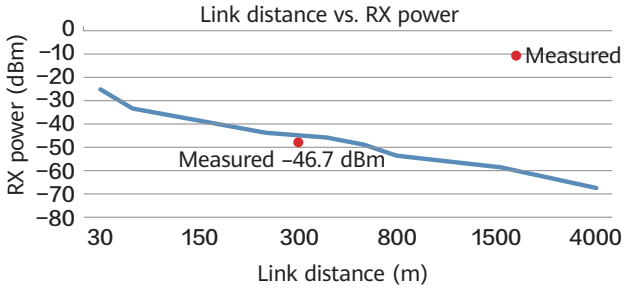

Figure 19 Receive power vs. Link distance

For medium distance outdoor transmission experiments over a distance of 330 m, we connected small 43 dBi lens antennas to the THz-wireless front-ends. At the receiver, the modem implements digital signal processing (DSP) to mitigate the effects of transmission impairments, considering both single-carrier and orthogonal frequency-division multiplexing (OFDM). The measurement results show different Baud rate from 4 GBd to 17.5 GBd. The reference curves correspond to a bit error rate (BER) at the experimentally used soft-decision forward error correction (SD-FEC) threshold of 2.1E-2, which can be achieved assuming error-free decoding with 20 percent overhead [59]. From the performance comparison results, single-carrier is better than OFDM since the former has a small peak-to-average ratio and is less sensitive to phase noise.

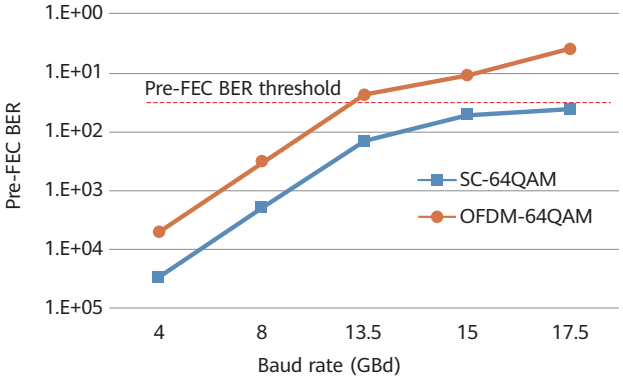

Figure 20 Pre-BER performance

Maximum throughput is 210 Gbit/s (17.5 x 4 x 2), and net data rate is 168 Gbit/s (210 x (1 – 0.2)). After removal of the forward error correction (FEC) overhead, the corresponding demodulated constellation is shown in Figure 21.

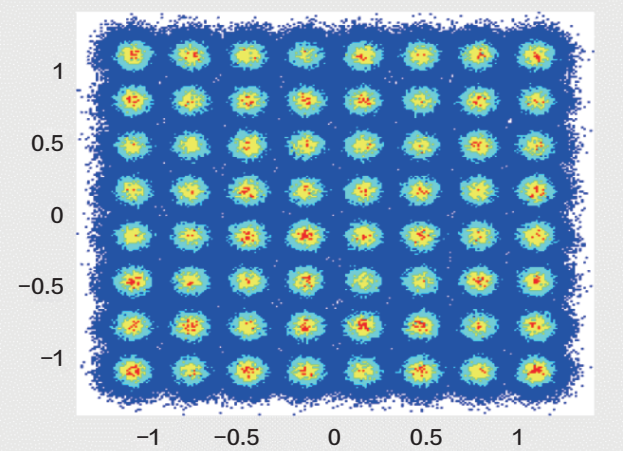

Figure 21 64QAM demodulated constellation

In addition, due to sufficient transmit power, high-gain antenna, and high-sensitivity DSP algorithm, the long distance field trial for single-input single-output (SISO) is also considered in our verification. As shown in Figure 22, the link distance is 3.6 km with high-humidity weather.

Figure 22 3.6 km long distance test

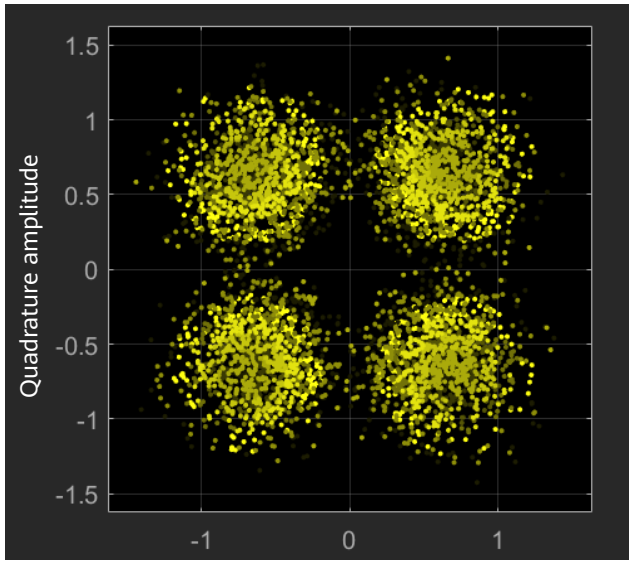

Figure 23 3.6 km, demodulation constellation

The corresponding link budget can be found in Table 5.

Table 5 Corresponding link budget

Parameter	Value
Frequency (GHz)	220
Symbol rate (Gbaud)	175
Transmitter EIRP [dBm]	50.5
Antenna gain [dBi]	42.0
Noise [dBm]	-71.7
RX power@3.6 km, dBm	-64.8

Maximum throughput is 35 Gbit/s, and net data rate is 28 Gbit/s after removal of the FEC overhead.

In order to explore the goal of realizing the ISAC in THz, we use a similar system architecture and device to carry out the sensing experiment. By using the concept of virtual MIMO and compression sensing algorithms, the EM imaging of metal objects hidden in a paper box is rebuilt successfully, and mm-level imaging resolution is achieved.

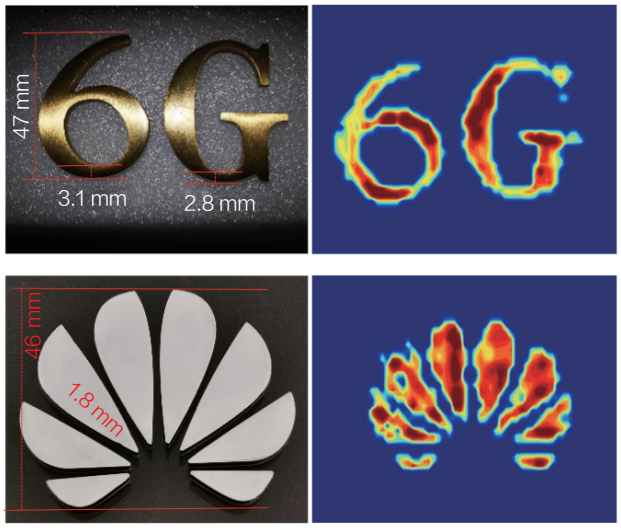

Figure 24 Imaging results of non-sparse full aperture scanning

5.2 THz Sensing System

Material characterization is a potential THz application that can be used to study properties of dielectric materials. The THz-TDS allows non-invasive measurement of various material parameters through some mathematical operations, which is by sending a broadband pulse signal to the material sample, and measuring the output signal either in transmission or reflection mode. We developed both simulation model and measurement setup for THz-TDS material characterization application.

CST Microwave Studio was used as simulation tool for THz-TDS setup. In the EM model as shown in Figure 25, two lens bow-tie antennas were designed and placed at each side of a dielectric Polytetrafluoroethylene (PTFE) sample. Then a time-domain simulator was set up and both simulations of with and without the sample were performed. After the simulation, both reference signal (without sample) and output signal (with sample), together with the input pulse, were collected and sent to an optimization algorithm to solve for the material properties, i.e., permittivity and loss tangent. Here, the Nelder-Mead algorithm was applied at each frequency to solve for the material property. It is shown that both permittivity and loss tangent extracted from the signal agree well with the theoretical values.

[60] demonstrated a quasi-optical system that performs complex material property measurement at sub-THz. As shown in Figure 25, a set of two-parabolic-mirror system and four parabolic-mirror system was developed. Two 80 mm-length corrugated horn antennas were designed to achieve a wide plane wave zone. After obtaining the S parameters at both ports, a closed mathematical form expression based on multiple reflection models was applied to calculate the complex material property. It is shown that the complex permittivity of various Rogers RT/duroid series printed circuit board (PCB) substrates had agreed well with the literature.

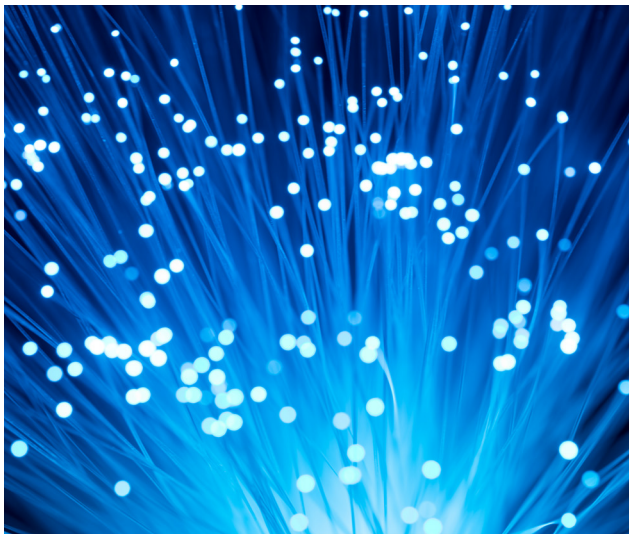

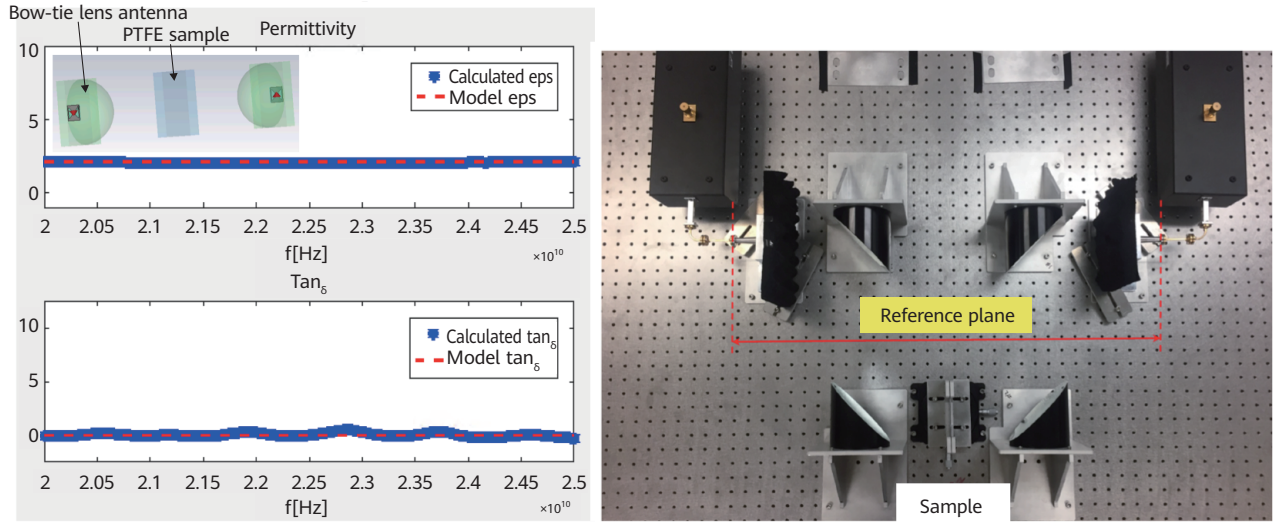

(a) EM simulation model and complex permittivity result

(b) Quasi-optical measurement system

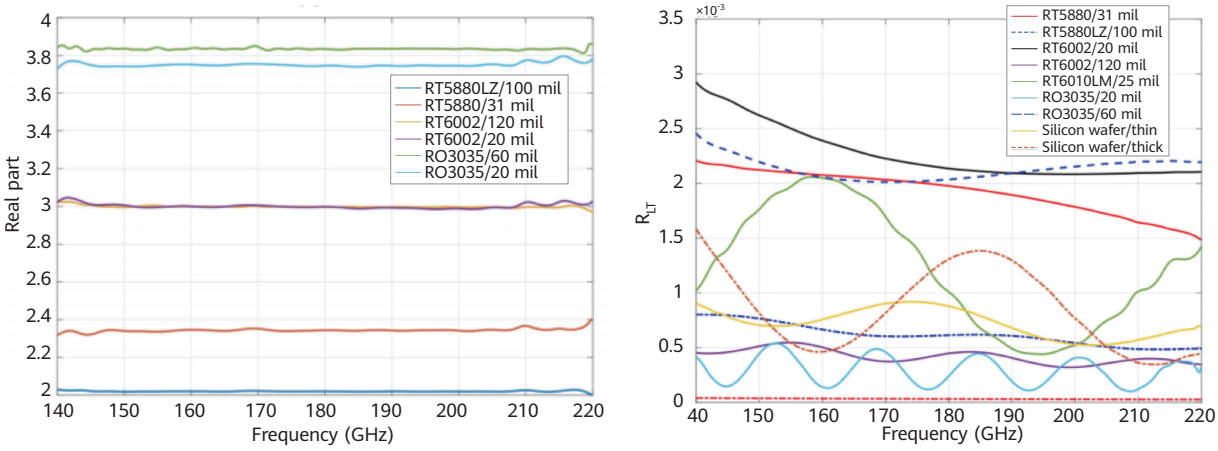

(c) (d) Measurement results of complex permittivity

Figure 25 Simulated and measurement results of material characterization application; measurement from [60]

THz imaging is promising for biomedical applications, due to the non-ionizing THz radiation. Fast and efficient image reconstruction algorithms can help accelerate the imaging acquisition speed. In this paper, a qualitative microwave holography (QMH) imaging method was demonstrated to perform the imaging and material mapping application [61–62]. QMH is a real-time direct inversion algorithm that can reconstruct the object image from all the S parameter measurements on the image plane. The S parameters are then used in two linearization models, Born's and Rytov's approximations, to reconstruct the object image and map its complex material property.

The following image test-bed was then set up to validate the QMH method, as shown in Figure 26. Nylon and metal balls of various sizes were set up, with diameters ranging from 1 mm to 3 mm and separation distance from 5 mm to 20 mm. Four S parameters were collected in 2-port measurements with frequency sweep from 26 GHz to 40 GHz. It is shown that QMH can achieve spatial resolution close to λ/4, even under a far field measurement setup. A comparison of Born and Rytov approximation in image qualities can be found in [62–63].

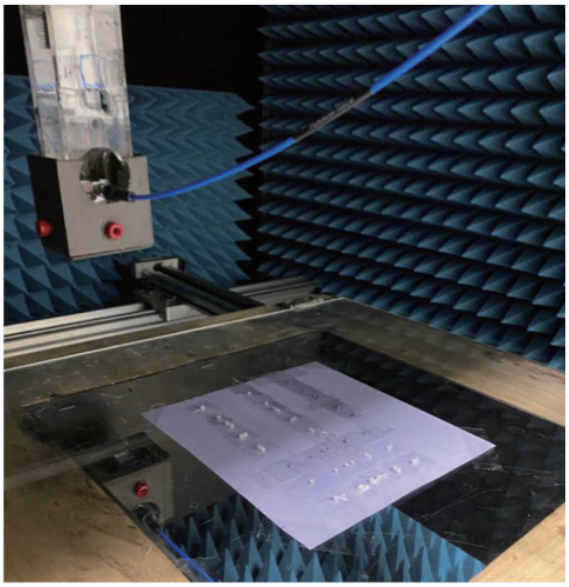

(a) QMH measurement setup

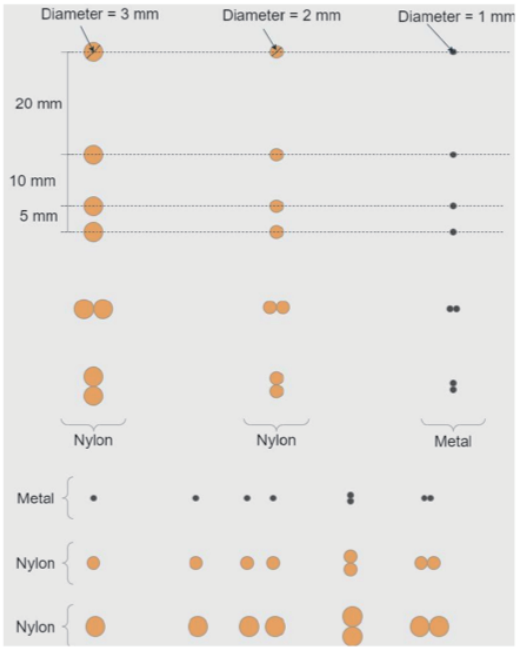

(b) Metal and nylon ball setup

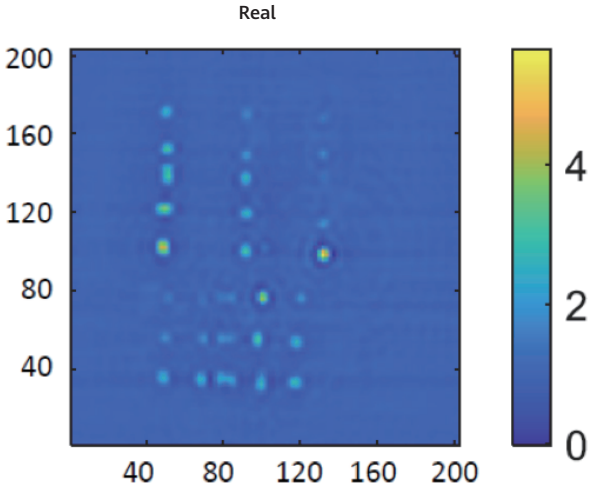

(c) Real part

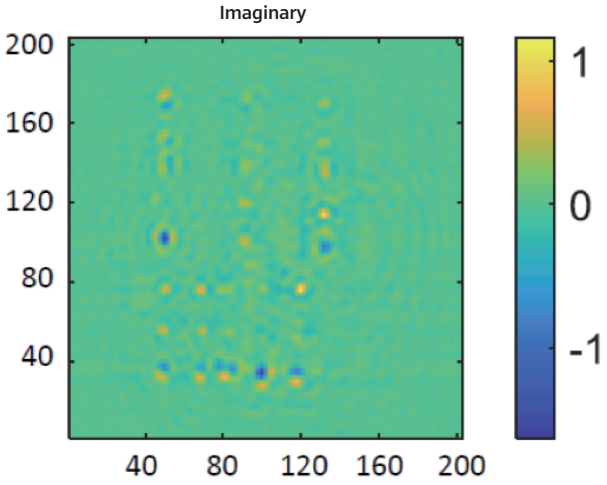

(d) Imaginary part of complex permittivity of reconstructed image

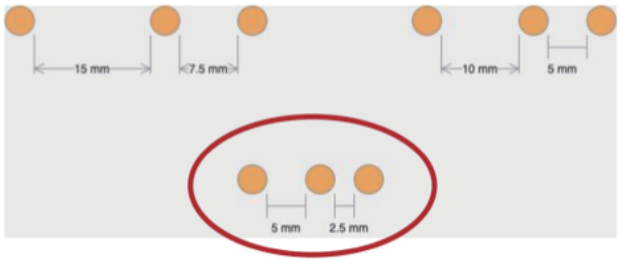

(e) Sub-wavelength ball separation setup

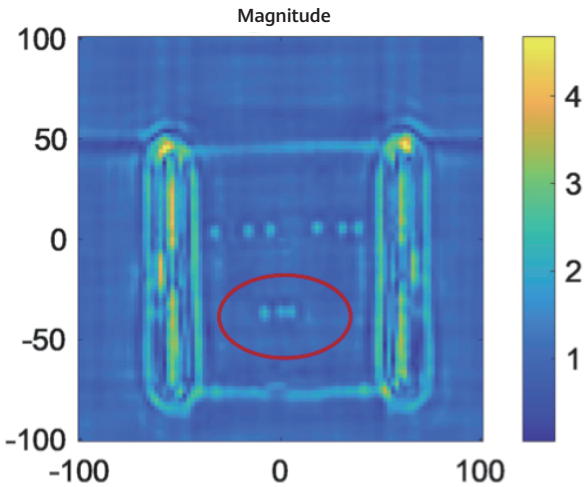

(f) Magnitude of complex permittivity of reconstructed image

Figure 26 QMH reconstruction of metal and nylon balls of various sizes. Results from [62]

6 Conclusion

In this paper, we discussed the advantages and typical scenarios of THz communication and sensing application. We also proposed a hybrid channel modeling framework to improve the modeling accuracy and efficiency at the THz frequency. In particular, the THz subsystem with silicon and III-V compound semiconductor materials heterogeneous integration is analyzed and proposed to improve the performance by using the advantage of different processes and materials. Finally, the prototype and measurement campaigns were conducted to illustrate the advantages of THz frequency for high throughput communication and high resolution sensing scenarios. A variety of measurement campaign examples show 210 Gbit/s data transmission rate at 330 m distance, and up to 3 mm invisible imaging, which achieves the highest performance in this field.

Future work will concentrate on following topics:

- Unified channel modeling frameworks and parameters compatible for all frequency bands and all application scenarios
- Unified air-interface and signal processing frameworks
- Technologies to improve the operating frequency and output power of components, and the low cost large array solutions at the THz frequency
- Real-time prototype and field trial with multiple points to further study the performance advantages of THz frequency for future 6G

References

[1] W. Tong and P. Zhu, "6G: the next horizon, from connected people and things to connected intelligence," Cambridge University Press, 2021.

[2] Zheng, Le, *et al*., "Radar and communication coexistence: an overview: a review of recent methods," *IEEE Signal Processing Magazine*, vol. 36, no. 5, pp. 85-99, 2019.

[3] Mazahir, Sana, Sajid Ahmed, and Mohamed-Slim Alouini, "A survey on joint communication-radar systems," 2020. https://doi.org/10.3389/frcmn.2020.619483.

[4] Li O, He J, Zeng K, *et al*., "Integrated sensing and communication in 6G A prototype of high resolution THz sensing on portable device," *2021 Joint European Conference on Networks and Communications & 6G Summit (EuCNC/6G Summit)*, 2021, pp. 544-549.

[5] Kürner T, "Turning THz communications into reality: status on technology, standardization and regulation," *2018 43rd International Conference on Infrared, Millimeter, and Terahertz Waves (IRMMW-THz)*. Nagoya, 2018, pp. 1-3.

[6] Tan Danny Kai Pin, *et al*., "Integrated sensing and communication in 6G: motivations, use cases, requirements, challenges and future directions," *2021 1st IEEE International Online Symposium on Joint Communications & Sensing (JC&S)*. IEEE, 2021.

[7] P. Almers, *et al*., "Survey of channel and radio propagation models for wireless MIMO systems," J Wireless Com Network, 2007.

[8] W. C. Chew, J. M. Jin, E. Michielssen, and J. Song, "Fast and efficient algorithms in computational electromagnetics," Boston, MA: Artech House, 2001.

[9] Sengupta K, Nagatsuma T, and Mittleman D M, "Terahertz integrated electronic and hybrid electronic-photonic systems," *Nature Electronics*, vol. 1, no. 12, pp: 622-635, 2018.

[10] Xu Y, Unseld F K, Corna A, *et al*., "On-chip integration of Si/SiGe-based quantum dots and switched-capacitor circuits," *Applied Physics Letters*, vol. 117, no. 14, 2020.

[11] Mokkapati S and Jagadish C, "III-V compound SC for optoelectronic devices," *Materials Today*, vol. 12, no. 4, pp: 22-32, 2009.

[12] Jia S, Zhang L, Wang S, *et al*., "2 × 300 Gbit/s line rate PS-64QAM-OFDM THz photonic-wireless transmission," *Journal of Lightwave Technology*, vol. 38, no. 17, pp: 4715-4721, 2020.

[13] Niu Z, Zhang B, Wang J, *et al*., "The research on 220GHz multicarrier high-speed communication system," *China Communications*, vol. 17, no. 3, pp: 131-139, 2020.

[14] Neu J and Schmuttenmaer C A, "Tutorial: an introduction to terahertz time domain spectroscopy (THz-TDS)," *Journal of Applied Physics*, vol. 124, no. 23, 2018.

[15] Final Acts WRC-19, https://www.itu.int/pub/R-ACT-WRC.14-2019.

[16] Technology trends of active services in the frequency range 275-3000 GHz, https://www.itu.int/pub/R-REP-SM.2352.

[17] Xianjin Li, Jia HE, Ziming Yu, *et al*., "Integrated sensing and communication in 6G: the deterministic channel models for THz imaging," pimrc 2021.

[18] He J, Chen Y, Wang Y, *et al*., "Channel measurement and path-loss characterization for low-terahertz indoor scenarios," arXiv preprint arXiv:2104.00347, 2021.

[19] Y. Chen, C. Han, Z. Yu, and G. Wang, "140 GHz channel measurement and characterization in an office room," ICC 2021 - IEEE International Conference on Communications, 2021, pp. 1-6, doi: 10.1109/ICC42927.2021.9500596.

[20] Y. Chen, Y. Li, C. Han, Z. Yu, and G. Wang, "Channel measurement and ray-tracing-statistical hybrid modeling for low-terahertz indoor communications," arXiv:2101.12436

[21] J. M. Ramirez *et al*., "III-V-on-silicon integration: from hybrid devices to heterogeneous photonic integrated circuits," *IEEE Journal of Selected Topics in Quantum Electronics*, vol. 26, no. 2, pp. 1-13, March-April 2020, Art no. 6100213, doi: 10.1109/JSTQE.2019.2939503.

[22] Mei, X. *et al*., "First demonstration of amplification at 1 THz using 25-nm InP high electron mobility transistor process," *IEEE Electron Dev. Lett*. 36, 327-329 (2015).

[23] Urteaga, M., Grifth, Z., Seo, M., Hacker, J. & Rodwell, and M. J. W, "InP HBT technologies for THz integrated circuits," *Proc. IEEE 105*, 1051-1067 (2017).

[24] Shinohara, K. *et al*., "Scaling of GaN HEMTs and Schottky diodes for submillimeter-wave MMIC applications," IEEE Trans. Electron Dev. 60, 2982-2996 (2013).

[25] A. Maestrini, J. Ward, J. Gill, H. Javadi, E. Schlecht, G. Chattopadhyay, F. Maiwald, N.R. Erickson, and I. Mehdi, "A 1.7 to 1.9 THz local oscillator source," *IEEE Microwave Wireless Compon. Lett*. 14 (6) (June 2004) 253-255.

[26] U. R. Pfeiffer, R. Jain, J. Grzyb, S. Malz, P. Hillger, and P. Rodríguez-Vízquez, "Current status of terahertz integrated circuits - from components to systems," *2018 IEEE BiCMOS and Compound Semiconductor Integrated Circuits and Technology Symposium (BCICTS)*, 2018, pp. 1-7, doi: 10.1109/BCICTS.2018.8551068.

[27] R. Han *et al*., "A SiGe terahertz heterodyne imaging transmitter with 3.3 mW radiated power and fully-integrated phase-locked loop," *IEEE Journal of Solid-State Circuits*, vol. 50, no. 12, pp. 2935-2947, 2015.

[28] Asada, M. and Suzuki, S., "Terahertz emitter using resonant-tunneling diode and applications," *Sensors* 2021, 21, 1384. https://doi.org/10.3390/s21041384.

[29] X. Li *et al*., "A 250-310 GHz power amplifier with 15-dB peak gain in 130-nm SiGe BiCMOS process for terahertz wireless system," in *IEEE Transactions on Terahertz Science and Technology*, doi: 10.1109/TTHZ.2021.3099057.

[30] Z. Griffith, M. Urteaga, P. Rowell, and R.Pierson, "A 23.2dBm at 210GHz to 21.0dBm at 235GHz 16-way PA-cell combined InP HBT SSPA MMIC," *in Proc. IEEE Compound Semiconductor IC Symp*., La Jolla, CA, USA, Oct. 2014, pp. 1-4.

[31] D. Parveg, D. Karaca, M. Varonen, A. Vahdati, and K. A. I. Halonen, "Demonstration of a 0.325-THz CMOS amplifier," *2016 Global Symposium on Millimeter Waves (GSMM) & ESA Workshop on Millimetre-Wave Technology and Applications*, 2016, pp. 1-3.

[32] Jiang, C. *et al*., "A fully integrated 320 GHz coherent imaging transceiver in 130 nm SiGe BiCMOS," *IEEE J. Solid State Circuits*, 51, 2596-2609 (2016).

[33] J. Moghaddasi and K. Wu, "Multifunction, multiband, and multimode wireless receivers: a path toward the future," *in IEEE Microwave Magazine*, vol. 21, no. 12, pp. 104-125, Dec. 2020, doi: 10.1109/MMM.2020.3023223.

[34] Hichem Guerboukha, Kathirvel Nallappan, and Maksim Skorobogatiy, "Toward real-time terahertz imaging," *Adv. Opt. Photon*. 10, 843-938 (2018).

[35] Z. Hu, M. Kaynak, and R. Han, "High-power radiation at 1 THz in silicon: a fully scalable array using a multi-functional radiating mesh structure," *in IEEE Journal of Solid-State Circuits*, vol. 53, no. 5, pp. 1313-1327, May 2018, doi: 10.1109/JSSC.2017.2786682.

[36] Z. Hu, C. Wang, and R. Han, "A 32-unit 240-GHz heterodyne receiver array in 65-nm CMOS with array-wide phase locking," *in IEEE Journal of Solid-State Circuits*, vol. 54, no. 5, pp. 1216-1227, May 2019, doi: 10.1109/JSSC.2019.2893231.

[37] S. N. Nallandhigal, P. Burasa, and K. Wu, "Deep integration and topological cohabitation of active circuits and antennas for power amplification and radiation in standard CMOS," *in IEEE Transactions on Microwave Theory and Techniques*, vol. 68, no. 10, pp. 4405-4423, Oct. 2020, doi: 10.1109/TMTT.2020.2997049.

[38] Liu, C., Ye, J., and Zhang, Y., "Thermally tunable THz filter made of semiconductors," *Opt. Comm*. 283, 865-868 (2010).

[39] Sanphuang, V., Ghalichechian, N., Nahar, N. K., and Volakis, J. L., "Reconfigurable THz filters using phase-change material and integrated heater," *IEEE Trans. THz. Sci*. Technol. 6, 583-591 (2016).

[40] Wu, X., Lu, H., and Sengupta, K., "Programmable terahertz chip-scale sensing interface with direct digital reconfiguration at sub-wavelength scales," *Nat Commun 10*, 2722 (2019). https://doi.org/10.1038/s41467-019-09868-6

[41] Venkatesh, S., Lu, X., Saeidi, H. *et al*., "A high-speed programmable and scalable terahertz holographic metasurface based on tiled CMOS chips," Nat Electron 3, 785-793 (2020). https://doi.org/10.1038/s41928-020-00497-2

[42] C. Huang *et al*., "Holographic MIMO surfaces for 6G wireless networks: opportunities, challenges, and trends," *in IEEE Wireless Communications*, vol. 27, no. 5, pp. 118-125, October 2020, doi: 10.1109/MWC.001.1900534.

[43] Venkatesh, S., Lu, X., Saeidi, H. *et al*., "A high-speed programmable and scalable terahertz holographic metasurface based on tiled CMOS chips," *Nat Electron 3*, 785-793 (2020). https://doi.org/10.1038/s41928-020-00497-2

[44] Qiang Jiang, Guofan Jin, and Liangcai Cao, "When metasurface meets hologram: principle and advances," *Adv. Opt. Photon*. 11, 518-576 (2019)

[45] Overvig, A.C., Shrestha, S., Malek, S.C. *et al*., "Dielectric metasurfaces for complete and independent control of the optical amplitude and phase," *Light Sci Appl* 8, 92 (2019). https://doi.org/10.1038/s41377-019-0201-7

[46] Pengfei Qiao, Li Zhu, and Connie J. Chang-Hasnain, "High-efficiency aperiodic two-dimensional high-contrast-grating hologram," *Proc. SPIE 9757, High Contrast Metastructures V*, 975708 (15 March 2016)

[47] X. Li, L. Chen, Y. Li, X. Zhang, M. Pu, Z. Zhao, X. Ma, Y. Wang, M. Hong, and X. Luo, "Multicolor 3D meta-holography by broadband plasmonic modulation," *Sci. Adv. 2*, e1601102 (2016).

[48] B. Wang, F. Dong, Q.-T. Li, D. Yang, C. Sun, J. Chen, Z. Song, L. Xu, W. Chu, Y.-F. Xiao, Q. Gong, and Y. Li, "Visible-frequency dielectric metasurfaces for multiwavelength achromatic and highly dispersive holograms," *Nano Lett*. 16, 5235-5240 (2016)

[49] H. Ren, G. Briere, X. Fang, P. Ni, R. Sawant, S. Héron, S. Chenot, S. Vézian, B. Damilano, V. Brändli, S. A. Maier, and P. Genevet, "Metasurface orbital angular momentum holography," *Nat. Commun*. 10, 2986 (2019)

[50] Gao Hui, Wang Yuxi, Fan Xuhao, Jiao Binzhang, Li Tingan, Shang Chenglin, Zeng Cheng, Deng Leimin, Xiong Wei, Xia Jinsong, and Hong Minghui, "Dynamic 3D meta-holography in visible range with large frame number and high frame rate," *Science Advances*. 6. eaba8595. 10.1126/sciadv.aba8595.

[51] T. Tajima, H. Song, and M. Yaita, "Compact THz LTCC receiver module for 300 GHz wireless communications," *in IEEE Microwave and Wireless Components Letters*, vol. 26, no. 4, pp. 291-293, April 2016, doi: 10.1109/LMWC.2016.2537044.

[52] S. Hu *et al*., "TSV technology for millimeter-wave and terahertz design and applications," *in IEEE Transactions on Components, Packaging and Manufacturing Technology*, vol. 1, no. 2, pp. 260-267, Feb. 2011, doi: 10.1109/TCPMT.2010.2099731.

[53] A. Hassona *et al*., "Demonstration of +100-GHz interconnects in eWLB packaging technology," IEEE Trans. Compon., Packag., Manuf. Technol.,vol. 9, no. 7, pp. 1406-1414, Jul. 2019.

[54] X. Yang *et al*., "Low-loss heterogeneous integrations with high output power radar applications at W-band," *in IEEE Journal of Solid-State Circuits*, doi: 10.1109/JSSC.2021.3106444.

[55] M. Urteaga *et al*., "THz bandwidth InP HBT technologies and heterogeneous integration with Si CMOS," *2016 IEEE Bipolar/BiCMOS Circuits and Technology Meeting (BCTM)*, 2016, pp. 35-41, doi: 10.1109/BCTM.2016.7738973.

[56] Peiying Zhu, "6GWFF 2021 - 6G: connected intelligence (keynote 1)," https://www.youtube.com/watch?v=PU0wKfwssk0.

[57] Coldrey M, "Modeling and capacity of polarized MIMO channels," VTC Spring 2008-IEEE Vehicular Technology Conference. IEEE, 2008: 440-4

[58] Kasdin N J, "Discrete simulation of colored noise and stochastic processes and 1/f/sup/spl alpha//power law noise generation," Proceedings of the IEEE, 1995, 83(5): 802-827.

[59] Koenig S, Lopez-Diaz D, Antes J, *et al*., "Wireless sub-THz communication system with high data rate," Nature Photonics 7, 2013, pp. 977-81.

[60] H. T. Zhu and K. Wu, "Complex permittivity measurement of dielectric substrate in sub-THz range," *in IEEE Transactions on Terahertz Science and Technology*, vol. 11, no. 1, pp. 2-15, Jan. 2021, doi: 10.1109/TTHZ.2020.3036181.

[61] Daniel Tajik, Aaron D. Pitcher, and Natalia K. Nikolova, "Comparative study of the Rytov and Born approximations in quantitative microwave holography," *Progress In Electromagnetics Research B*, Vol. 79, 1-19, 2017.

[62] D. Tajik and N.K. Nikolova, "Real-time imaging with simultaneous use of Born and Rytov approximations in quantitative microwave holography," *IEEE Trans. Microwave Theory Tech*. (submitted Aug. 9, 2021)

[63] D. Tajik, R. Kazemivala, and N.K. Nikolova, "Combining the Born and Rytov approximations in

quantitative microwave holography," *The IEEE 19th Int. Symp. on Antenna Technology and Applied Electromagnetics (ANTEM 2021)*, Winnipeg, Canada, Aug. 8-11, 2021.